

How Much Energy Is Transferred from the Winds to the Thermocline on ENSO Time Scales?

JACLYN N. BROWN* AND ALEXEY V. FEDOROV

Department of Geology and Geophysics, Yale University, New Haven, Connecticut

(Manuscript received 3 November 2008, in final form 18 August 2009)

ABSTRACT

The dynamics of El Niño–Southern Oscillation (ENSO) are studied in terms of the balance between energy input from the winds (via wind power) and changes in the storage of available potential energy in the tropical ocean. Presently, there are broad differences in the way global general circulation models simulate the dynamics, magnitude, and phase of ENSO events; hence, there is a need for simple, physically based metrics to allow for model evaluation. This energy description is a basinwide, integral, quantitative approach, ideal for intermodel comparison, that assesses model behavior in the subsurface ocean. Here it is applied to a range of ocean models and data assimilations within ENSO spatial and temporal scales. The onset of an El Niño is characterized by a decrease in wind power that leads to a decrease in available potential energy, and hence a flatter thermocline. In contrast, La Niña events are preceded by an increase in wind power that leads to an increase in the available potential energy and a steeper thermocline. The wind power alters the available potential energy via buoyancy power, associated with vertical mass fluxes that modify the slope of the isopycnals. Only a fraction of wind power is converted to buoyancy power. The efficiency of this conversion γ is estimated in this study at 50%–60%. Once the energy is delivered to the thermocline it is subject to small, but important, diffusive dissipation. It is estimated that this dissipation sets the e -folding damping rate α for the available potential energy on the order of 1 yr^{-1} . The authors propose to use the efficiency γ and the damping rate α as two energy-based metrics for evaluating dissipative properties of the ocean component of general circulation models, providing a simple method for understanding subsurface ENSO dynamics and a diagnostic tool for exploring differences between the models.

1. Introduction

Over the last several decades significant progress has been made in explaining and modeling El Niño–Southern Oscillation (ENSO), which is the dominant mode of climate variability in the tropical Pacific induced by ocean–atmosphere interactions (e.g., Wang et al. 2004; McPhaden et al. 2006; Fedorov and Brown 2009). Despite these efforts, broad discrepancies still persist in the way ENSO is simulated, particularly in the subsurface (AchutaRao and Sperber 2006; Guilyardi et al. 2009). For example, the present suite of global circulation models includes

very different magnitudes and frequency spectra for ENSO variability and different representation of physical mechanisms such as thermocline and SST modes (Fedorov and Philander 2001; Guilyardi 2005).

From the point of view of ocean dynamics, El Niño and its complement La Niña manifest as a horizontal redistribution of warm water along the equator, altering the slope of the thermocline. During La Niña years, strong zonal winds pile up warm water in the west, causing the thermocline to develop a large east–west slope. During an El Niño, weakened zonal winds permit warm water to advect to the east so that the thermocline becomes more horizontal. The same phenomena can be understood by considering the balance of mechanical energy in the tropical ocean during the ENSO cycle—notably, the transfer of energy from the winds to the thermocline prior to La Niña, a removal of energy prior to El Niño, and energy dissipation by various oceanic processes. These energy transformations are the focus of the present paper.

* Current affiliation: CSIRO Wealth from Oceans National Research Flagship, Hobart, Tasmania, Australia.

Corresponding author address: Jaclyn N. Brown, Centre for Australian Weather and Climate Research, Hobart, Tasmania, Australia 7000.

E-mail: jaci.brown@csiro.au

The budget of potential and kinetic energy for the tropical ocean is given by two simple equations (Goddard and Philander 2000; Brown and Fedorov 2008), formulated here in terms of anomalies with respect to the climatological state (in such a formulation all variables, including dissipation anomalies, can be both negative or positive):

$$\frac{\partial K}{\partial t} = W - B - D_1, \quad (1)$$

$$\frac{\partial E}{\partial t} = B - D_2. \quad (2)$$

Detailed explanations of these equations and their derivation are provided in section 2 and appendix A. Here we give a brief overview to aid discussion: Anomalous wind power (W) is generated as wind supplies (removes) energy to the ocean by acting in the same (opposite) direction to the surface currents [see Eq. (1) and Fig. 1]. The wind power is calculated from the surface wind stress and the ocean surface currents. A significant fraction of anomalous wind power is converted to buoyancy power anomalies (B) associated with vertical mass fluxes that distort ocean isopycnals. Because changes in kinetic energy (K) are negligible (not more than a few percent of available potential energy variations), the remaining wind power goes directly into D_1 . We loosely define D_1 as viscous dissipation, but in reality it represents several different types of energy loss, including advection of energy out of the tropical basin. A negative dissipation anomaly means that there is actually less dissipation in the system compared to mean values. A full discussion of this dissipation term is contained in the appendix.

Further, the buoyancy power affects the rate of change of available potential energy (E), with a relatively small dissipation anomaly D_2 [see Eq. (2)]. Thus, the buoyancy power B acts a conversion term responsible for converting wind power into available potential energy. The dissipation term, D_2 , loosely defined as diffusive dissipation, combines the effects of thermal and freshwater fluxes, energy advection, diffusion, and shear in the stability profile.

It is important that in the tropical Pacific, the available potential energy is largely a measure of the thermocline slope along the equator (e.g., Fedorov et al. 2003; Brown and Fedorov 2008), which is why this analysis so readily lends itself to studying ENSO (as first suggested by Goddard and Philander 2000). A steep thermocline (as during La Niña) implies a positive energy anomaly, and a flat thermocline (El Niño) implies a negative energy anomaly. According to Eq. (2), these variations in E are caused by prior anomalies (positive or negative, re-

spectively) in buoyancy power induced by wind power anomalies. Schematically, the process of altering E stored in the thermocline is shown in Fig. 1.

One of the central goals of this paper is to quantify the role of dissipation in the energy balance of the tropical Pacific Ocean, as described by Eqs. (1) and (2) on time scales relevant for ENSO, and at the same time to develop energy-based metrics for intermodel comparisons. As the available observational subsurface density data are limited, we will evaluate these metrics in a number of ocean-only models and data assimilations to define a baseline for further use in coupled general circulation models.

As a corollary of this study, we will show that variations in the available potential energy of the tropical ocean can be described with good accuracy as

$$\frac{\partial E}{\partial t} = \gamma W - \alpha E, \quad (3)$$

a combination of Eqs. (1) and (2). Here, we have introduced the efficiency γ of the conversion of wind power W into buoyancy power B and the e -folding damping rate α of available potential energy anomalies E . We will show that ocean models and data assimilations indicate that γ ranges between approximately 50% and 60%. The e -folding damping time scale of the available potential energy anomalies, α^{-1} , is estimated here at 1 year. Typically the damping scale for thermocline depth anomalies is on the order of 2 years, consistent with the previous study of Fedorov (2007); see appendix B.

This description of ENSO, based on exact energy conservation laws, has some similarities with the recharge–discharge oscillator model (Jin 1997; Meinen and McPhaden 2000); however, it has the advantage of being a basinwide, quantitatively rigorous approach that can be applied to any model, over any time period, for any time scale. Indeed, ocean general circulation models that describe ENSO events are as complex as the ocean itself. Idiosyncrasies of different models introduce further complicating factors as we try to understand why models produce ENSO events in different ways. Ocean energetics provides a physically sound way to compare the models without having to account for many of the model differences.

In this study we use our energy-based analysis as a diagnostic tool for understanding some differences in the way that ocean models simulate ENSO, such as wind strength anomalies, thermocline depth variability, and the damping rate of ENSO. In particular, we explore how models applying different wind stress forcing can still generate El Niño events of similar magnitude. This

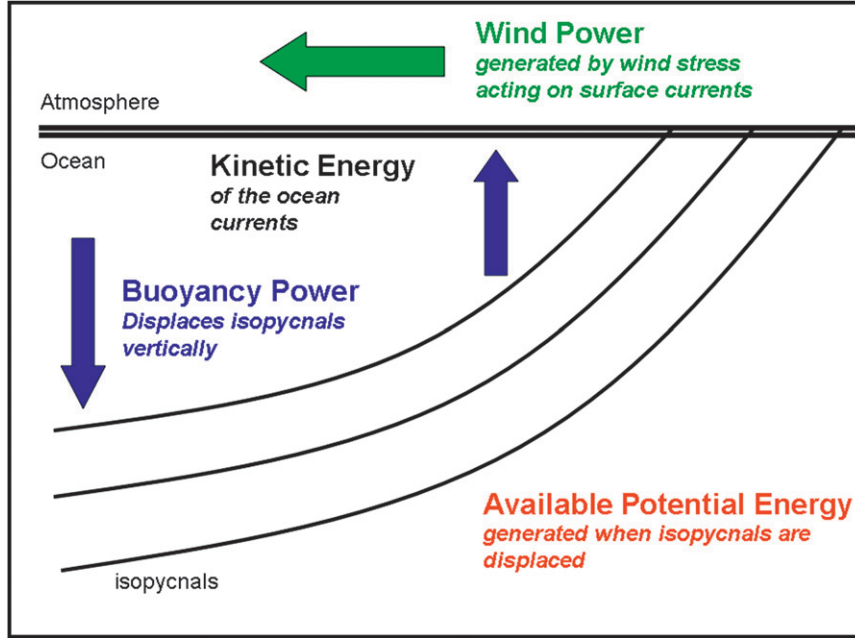


FIG. 1. A schematic of the energy transfer in the tropical Pacific Ocean relevant to ENSO. Wind power (i.e., the rate of work, W) is generated by the wind stress acting on surface currents. The wind power modifies the kinetic energy of ocean currents but is mainly converted to buoyancy power B . The buoyancy power causes vertical displacement of the isopycnals, which changes the available potential energy E . The available potential energy calculated for the tropical Pacific Ocean is largely a measure of the thermocline slope along the equator.

means that models with larger wind power anomalies must be dissipating that energy in larger quantities to achieve the same final result. Our metrics will help us understand these differences and use them as indicators of how different model features (such as parameterizations of friction and diffusion or the wind stress structure) can affect the outcome of ENSO simulations. In our companion paper (Brown et al. 2009, manuscript submitted to *Climate Dyn.*, hereafter BRO), we utilize the metrics established here to compare the leading models from the Intergovernmental Panel for Climate Change Fourth Assessment Report (IPCC AR4) model intercomparison.

This study follows on from Brown and Fedorov (2008), who explored the mean state of the energy balance in the tropical Pacific in the same ocean-only models, data assimilations, and coupled models. They found that on average approximately 0.2 to 0.4 TW ($1 \text{ TW} = 10^{12} \text{ W}$) of wind power is generated in the tropical Pacific in the ocean models and 0.3 to 0.6 TW in the coupled models. The amount of wind power depends on the strength of the wind stress product used and the model representation of the surface currents, particularly the North Equatorial Countercurrent. On average, 10%–20% of the mean wind power is transferred to the subsurface ocean to maintain the mean thermocline slope. The present study

extends this analysis to consider interannual anomalies to the mean climatology.

2. Calculating the energetics

The main part of this study uses a run from the Nucleus for European Modeling of the Ocean (NEMO) ocean model [the ORCA05 version from L’Institut Pierre-Simon Laplace (IPSL)] forced with National Centers for Environmental Prediction–National Center for Atmospheric Research (NCEP–NCAR) reanalysis winds. We will refer to this model as ORCAa. We then compare the results with version 4 of the Modular Ocean Model (MOM4) and the Parallel Ocean Program (POP) ocean model and a different run of the ORCA model forced with 40-yr European Centre for Medium-Range Weather Forecasts (ECMWF) Re-Analysis (ERA-40) winds (ORCAb). We will also analyze two data assimilation products, Estimation of the Circulation and Climate of the Ocean (ECCO) and the Global Ocean Data Assimilation System (GODAS). Specifics of these models and data assimilations are shown in Table 1 and are discussed in Brown and Fedorov (2008). In each case we use monthly averages to calculate our energy metrics. Analysis with weekly data was tried and showed higher levels of wind

TABLE 1. Comparison of the four ocean model runs and two data assimilations used in this study: ORCAa, ORCAb, MOM4, POP, ECCO, and GODAS.

Model	ORCAa	ORCAb	MOM4	POP	GODAS	ECCO
Simulation period	1964–2000	1964–2000	1960–2001	1960–2000	1980–2005	1992–2004
Spatial resolution	$0.5^\circ \times 0.5^\circ$	$0.5^\circ \times 0.5^\circ$	$1^\circ \times \frac{1}{3}^\circ$	$1.125^\circ \times \frac{1}{4}^\circ$	$1^\circ \times \frac{1}{3}^\circ$	$1^\circ \times 1^\circ$
near equator						
Wind stress	NCEP–NCAR reanalysis	ERA-40	NCEP–NCAR reanalysis	NCEP–NCAR reanalysis + satellite products. Maltrud and McClean (2005)	Momentum, heat, and freshwater fluxes from NCEP atmospheric reanalysis 2.	NCEP/NCAR reanalysis
product					Temperature and salinity are also assimilated.	
					27	
Vertical levels in the top 400 m	20	20	30	18	10	
Vertical tracer diffusion	Turbulent closure model (Blanke and Delecluse 1993)	Turbulent closure model (Blanke and Delecluse 1993)	KPP scheme (Large et al. 1994), includes Bryan and Lewis (1979) background mixing.	KPP scheme	KPP scheme	KPP scheme
Horizontal tracer mixing	Gent–McWilliams and Laplacian lateral isopycnal diffusion.	Gent–McWilliams and Laplacian lateral isopycnal diffusion.	Gent–McWilliams stirring and biharmonic rotated scheme (Griffies et al. 2005)	Gent–McWilliams isoneutral mixing scheme.	Gent–McWilliams isoneutral mixing scheme.	Gent–McWilliams–Redi
Reference	Barnier et al. (2006)	Barnier et al. (2006)	Griffies et al. (2006)	Collins et al. (2006)	Behringer (2007)	Wunsch and Heimbach (2007)

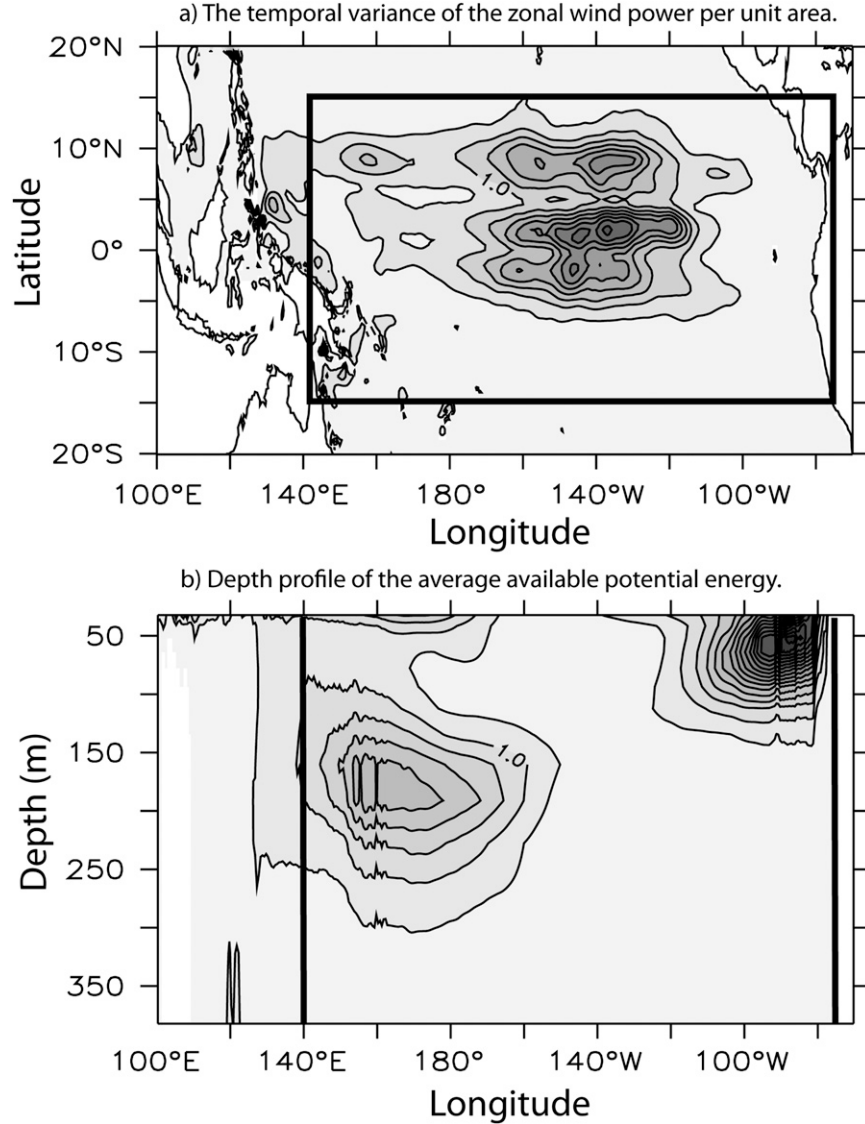


FIG. 2. Variance per unit area of (a) the monthly zonal wind power W (10^4 W m^{-2}) and (b) the monthly average available potential energy \bar{E} (10^{19} J m^{-2}) for the ORCAa run, before the integration. The seasonal cycle was removed from the original data. The contour interval is 0.5 for both panels. The region chosen for energy calculations is shown as the thick black rectangle: 15°S – 15°N , 140°E – 80°W , 0–400 m. When basinwide integrals are calculated, a mask is applied to remove land and to block out contributions from the Gulf of Carpentaria and the Caribbean Sea.

power generation, suggesting that we are undersampling. Such high-resolution model output, while ideal, is not always available.

The three critical variables in the energy balance of Eqs. (1) and (2) are wind power (W), buoyancy power (B), and available potential energy (E). As mentioned before, the rate of change of kinetic energy is negligible. Following previous studies (Goddard and Philander 2000; Fedorov et al. 2003; Fedorov 2007; Brown and Fedorov 2008), we calculate these variables as follows.

The wind power (in watts) is defined as the dot product of the wind stress, $\tau = (\tau^x, \tau^y)$, and the surface current $\mathbf{u} = (u, v)$, integrated over the surface A of the tropical Pacific basin (black rectangle, Fig. 2a):

$$W = \iint \mathbf{u} \cdot \tau dA. \quad (4)$$

Note that previous studies (e.g., Dawe and Thompson 2006; Zhai and Greatbatch 2007) have shown that it is

important to include the ocean surface currents in the wind stress formulation.

It is not uncommon that in calculating the wind power, surface currents are separated into geostrophic and ageostrophic components. Away from the equator, it has been argued that it is the wind power acting on the geostrophic currents that supplies energy to the interior of the ocean (Weijer and Gille 2005; Wang and Huang 2004), while the wind work done on ageostrophic flow is dissipated. This separation is impossible in the vicinity of the equator because the Coriolis parameter vanishes and because large nonlinear advection terms become important for the dynamical balance (Brown et al. 2007). For these reasons, we define the wind power as the wind stress multiplied by the full surface current.

To capture ENSO temporal and spatial scales, we consider the ocean energy balance over a limited region in the tropical Pacific. The boundaries of this region are chosen to encompass most of the variations in wind power and available potential energy. Based on the arguments outlined below, we have decided to use the region 15°S–15°N, 140°E–70°W, and 0 to 400 m (black rectangles, Fig. 2b). We apply a mask to the region to remove any signal that comes from the Caribbean Sea and the Gulf of Carpentaria. Our box is extended to 70°W to ensure that we include thermocline variability along the coast of South America. Higher-resolution models are able to capture more of the wind power variability in strong western boundary currents, but this contribution remains small compared to the large source of energy in the central and eastern equatorial Pacific.

A significant fraction of the wind power is converted to buoyancy power (in watts), defined as

$$B = \iiint (\rho - \rho^*) g w dV, \quad (5)$$

where the integral is taken over the volume V of the tropical Pacific basin in the upper ocean (Fig. 2b). Here, w is the vertical velocity, g is gravity, and ρ is potential density. The horizontal average ρ^* is the reference potential density obtained by averaging ρ over x , y , and t in the basin of interest.

The available potential energy is defined in terms of potential density, according to Oort et al. (1989), as

$$E = \iiint \frac{1}{2} \frac{(\rho - \rho^*)^2}{S^2} dV, \quad (6)$$

with a stability factor

$$S^2 = \left| \frac{\rho_z^*}{g} \right|,$$

which is proportional to the buoyancy frequency. It is important to use potential density in this calculation, rather than in situ density, since their vertical gradients are significantly different.

Seasonal variations in the energy balance are considerably weaker than interannual. In fact, for many models and data assimilations, seasonal changes do not typically exceed 10%–20% of interannual changes (A. Fedorov et al. 2010, unpublished manuscript). Nevertheless, the seasonal cycle should be removed for our analysis, so that after obtaining E , W , and B we calculate the annual cycle and subtract it from these variables.

Spatially, most of the ENSO signal in available potential energy occurs in our bounding box (Fig. 2b). Even though the wind power signal appears in the central Pacific right up to 15°N (Fig. 2a), its largest influence on the buoyancy power, and hence available potential energy, is along the equator (Brown and Fedorov 2008).

It is tempting to extend the region of interest westward to include the region along the coast of the Philippines, but we found that the inclusion of this region adds little to the available potential energy signal. Moreover, extending the box this far west would highlight differences in the way models represent the current structure here, dissipation in the strong western boundary currents, and contributions from the meridional wind stress, rather than the equatorial dynamics.

To calculate available potential energy, we have chosen the vertical range of integration from the surface to 400 m because it ensures that most of the thermocline variations are captured (Fig. 2b). Goddard and Philander (2000) used 30 m (the typical depth of the mixed layer) as the upper limit in their integration. They decided on this upper limit because the expression for the available potential energy is divided by $d\rho^*/dz$. This term can become very small within the mixed layer, giving too much weight to surface variations. In our study, we find that this is not a problem for the interannual signal, even when the calculations extend up to the first model level at 5-m depth. By integrating to the top level we are able to incorporate some of the thermocline variations that occur in the far eastern Pacific above the 30-m depth. In addition, integrating to the surface makes this method easily applied to models with different mixed layer depths.

3. Robust features of the energy balance

Consistent with previous studies and similar to the mean energy balance, interannual variations in wind power are clearly dominated by the zonal component of the wind power. In fact, the variance of the zonal component (thin line, Fig. 3a) can be ~45 times greater than the meridional

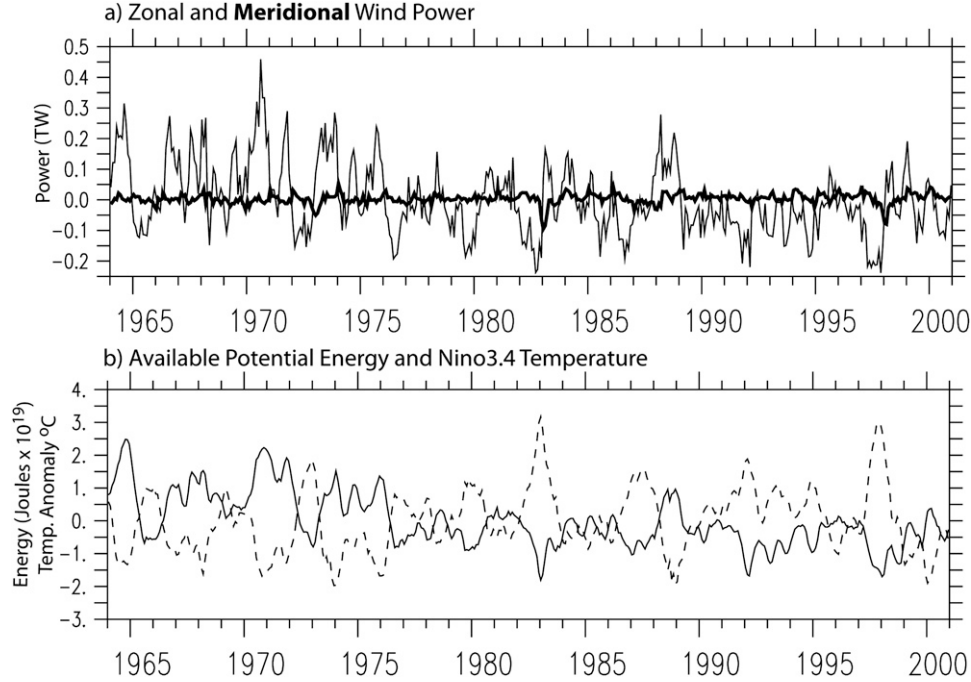


FIG. 3. (a) Interannual anomalies for the zonal (thin line) and meridional (thick line) contributions to wind power (TW) for the ORCAa run. (b) Interannual variations in available potential energy (solid line) and Niño-3.4 temperature anomalies (dashed line) for the ORCAa run. The two variables are anti-correlated at -0.77 , which is significant at the 95% level.

(thick line) (see also Wunsch 1998). Further, we will neglect the meridional component because variability in the meridional wind power comes from strong coastal currents and aligned wind stress associated with western boundary currents (also found by Wunsch 1998). We note here that on seasonal time scales, which are not considered in this study, the meridional wind power can potentially become significant for the energy balance.

The wind power exhibits a strong interannual signal, with the W anomaly fluctuating between negative values prior to El Niño years (e.g., 1982 and 1997) and positive values prior to La Niña (e.g., 1970, 1988 and 1998; Fig. 3a). Note that the total wind power (mean plus anomaly) integrated over the tropical area is always positive, regardless of the large negative anomalies that are generated. The strength of the interannual wind power is not simply attributable to the strength of the zonal winds; rather, it depends on a complex relationship involving both the mean and anomalies in the surface currents (Goddard and Philander 2000).

In all models, the available potential energy anomaly anticorrelates strongly with Niño-3.4 temperatures (Fig. 3b, correlation coefficient of -0.77 for the ORCAa model). This is because on ENSO time scales the available potential energy is dominated by changes in the thermocline slope along the equator. The available potential

energy is a measure of the thermocline slope because it is a basinwide integral of the density anomaly, independent of the density that the thermocline occurs at. In the mean, there is a tight connection between the level of wind power and the mean slope of the thermocline (Brown and Fedorov 2008).

Equations (1) and (2) can be combined by eliminating buoyancy power to give

$$\frac{\partial E}{\partial t} = W - D_1 - D_2 \quad (7)$$

which describes a direct relationship between wind power and available potential energy (Fedorov 2007). If there were no dissipation, these two terms would be exactly 90° or ~ 1 year out of phase. The observed phase lag between the two, which lagged correlation analysis shows to be approximately 6 months, is actually smaller (Fig. 4a), indicating that the dissipation is indeed important.

In a similar manner to the recharge-discharge oscillator, the ENSO cycle can be viewed on a phase plane with E and W as phase coordinates (Fig. 4b). This appears to be a more quantitative representation of ENSO dynamics than the recharge oscillator, as it is a basinwide integration of energy. The recharge oscillator is more

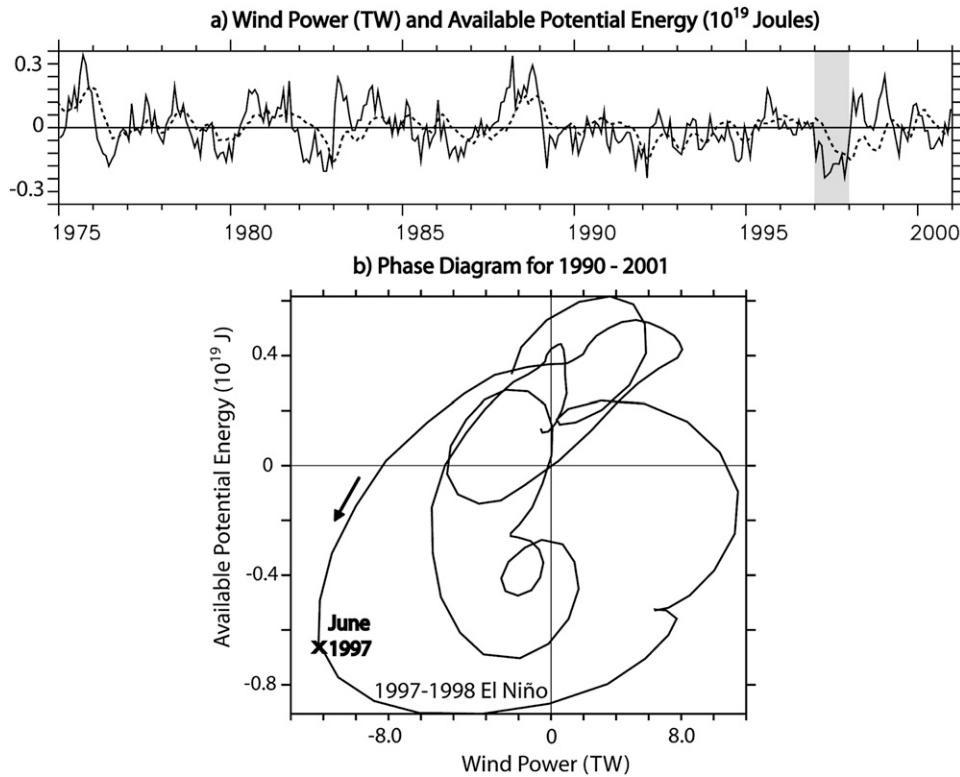


FIG. 4. (a) The zonal wind power (solid line, TW) and available potential energy (dashed line, 10^{19} J), smoothed with a five-point running mean. Wind power leads the available potential energy by approximately 6 months. Shading indicates changes in the wind power preceding El Niño of 1997. (b) A phase diagram (a phase plane) of monthly wind power and the available potential energy for the period 1990–2001, smoothed with an 11-point triangle filter. The prominent excursion of the phase trajectory into the lower half plane corresponds to the 1997/98 El Niño.

subjective because models have differing thermocline depths and mean temperatures. The energetics analysis can be applied to any model, over any time period, and without worrying about specific model “flavors” of ENSO, such as eastern Pacific or central Pacific El Niños (Kao and Yu 2009).

4. Quantifying energy dissipation

a. Kinetic energy balance

The first instance when energy loss becomes important is in the kinetic energy balance, mainly through the loss of wind power when it is converted to buoyancy power. We will show here that only about half of the wind power into the ocean is converted to buoyancy power as described by Eq. (1). To account for this energy loss, we introduce a measure—we call it the efficiency γ —to describe the proportion of the wind power being converted to buoyancy power. The efficiency is estimated as the least squares fit between the wind power and the buoyancy power (after a 5-point smoothing filter has been applied to the monthly data):

$$\gamma = \frac{\langle BW \rangle}{\langle W^2 \rangle} \quad (8)$$

The smoothing is applied to highlight the ENSO-like variability and remove higher-frequency signals.

We find an extremely high correlation between the wind power and buoyancy power (0.95 in the case of the ORCAa model), which indicates the buoyancy power is indeed a means to transfer energy directly from the wind to the ocean interior. The efficiency of this transfer, however, is not very large and is estimated at 54% for ORCAa.

Where do the excess energy anomalies go (roughly half of the wind power anomalies)? Since variations in kinetic energy are tiny, this energy must be dissipated [Eq. (1)]. Such a high level of energy loss is not surprising. Goddard and Philander (2000) argued that some of the kinetic energy is lost because of work done against the pressure gradient by the ageostrophic current (Fig. 5b, red line), represented by P in Eq. (A4) of appendix A. This term, however, represents only a small fraction of the energy loss. The main energy loss actually results

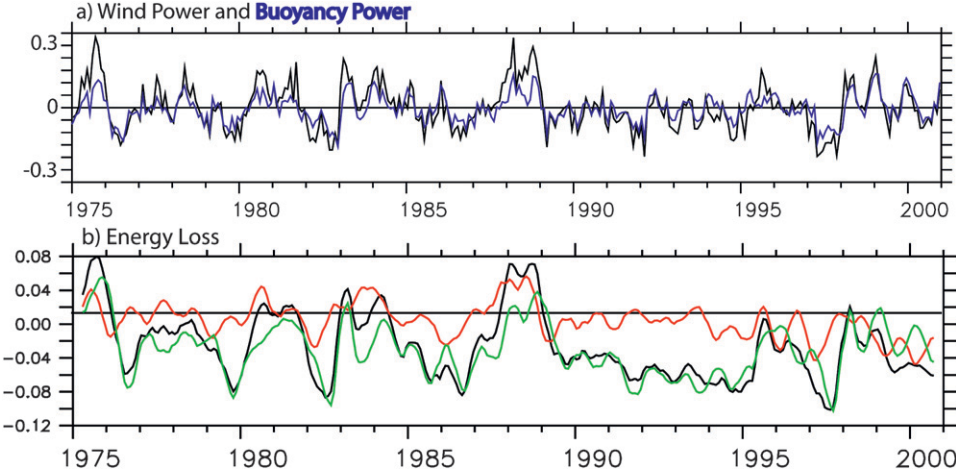


FIG. 5. The main components of the energy balance in Eq. (1) for the ORCAa model. (a) Time series of the monthly anomalies of zonal wind power (black line, TW) and buoyancy power (blue line, TW). The two variables are highly correlated, while the difference between the two indicates that only a fraction of wind power is converted to buoyancy power. (b) The total energy loss from wind power to buoyancy power (TW) is shown by the black line [calculated as the difference between the two time series in the top panel and defined as D_1 in Eq. (1)]. This total energy loss D_1 is separated into the loss from the work done on the pressure gradient by the ageostrophic flow (red line) and the remaining dissipation anomaly (green line) induced mainly by vertical and horizontal friction (see appendix A).

from vertical and horizontal friction [Fig. 5, green line; see also appendix A and some discussion in Goddard and Philander (2000)].

The efficiency of the wind power to buoyancy power transfer varies among the models in the range of 40%–60% (Fig. 6 and Table 2). The POP model is a particular outlier with an efficiency of only 38%. At the other end of the scale, the MOM4 model has a high efficiency of 64%. MOM and ORCAa were forced with a similar wind stress but have different efficiencies, demonstrating that efficiency is a product of the model, not just the forcing.

The ORCA model runs are an interesting case study. The two runs are of the same model but use different wind stresses. In fact, the ORCAa forcing has stronger wind stress variability than ORCAb, yet they have similar efficiencies. This means that more energy is going into the subsurface in the ORCAa run than in ORCAb. This result will be discussed further in the next sections.

b. Available potential energy balance

The rate of change of available potential energy is mostly controlled by the buoyancy power B [Eq. (2); Fig. 7]. The available potential energy lags the buoyancy power by roughly 6 months (Fig. 7a), similar to its lag from the wind power. The difference between the rate of change of available potential energy and B is a relatively small dissipation term D_2 (Fig. 7b) describing direct dissipa-

tion of the available potential energy anomalies [see appendix A and Griffies (2004) for a full discussion of potential and internal energy transformations].

In the absence of the wind forcing, one would expect that the damping of a given available potential energy anomaly would be proportional to the anomaly itself, giving an exponential decay of the anomaly amplitude (as explored by Fedorov 2007). For example, in a La Niña year, the damping of the thermocline slope anomaly would act to reduce the thermocline slope back to its mean position (e.g., by anomalous surface heating of the cold tongue). This representation of dissipation has a simple physical meaning: all damping processes effectively tend to restore the state of the ocean toward the state with a minimum anomalous available potential energy. The greater the anomalies associated with ENSO are, the stronger the restoring force is.

Therefore, we have assumed that the dissipation term D_2 is proportional to the available potential energy anomaly and equals αE , where α^{-1} can be thought of as an e -folding time scale of the available potential energy damping (also see Fedorov 2007). A number of different processes contribute to this damping rate, such as turbulent diffusion, generation of tropical instability waves, generation of equatorial Kelvin and Rossby waves, advection of energy out of the basin, and damping by surface heat fluxes. On the whole, the damping time scale α^{-1} gives an integral parameter that accounts for these different processes.

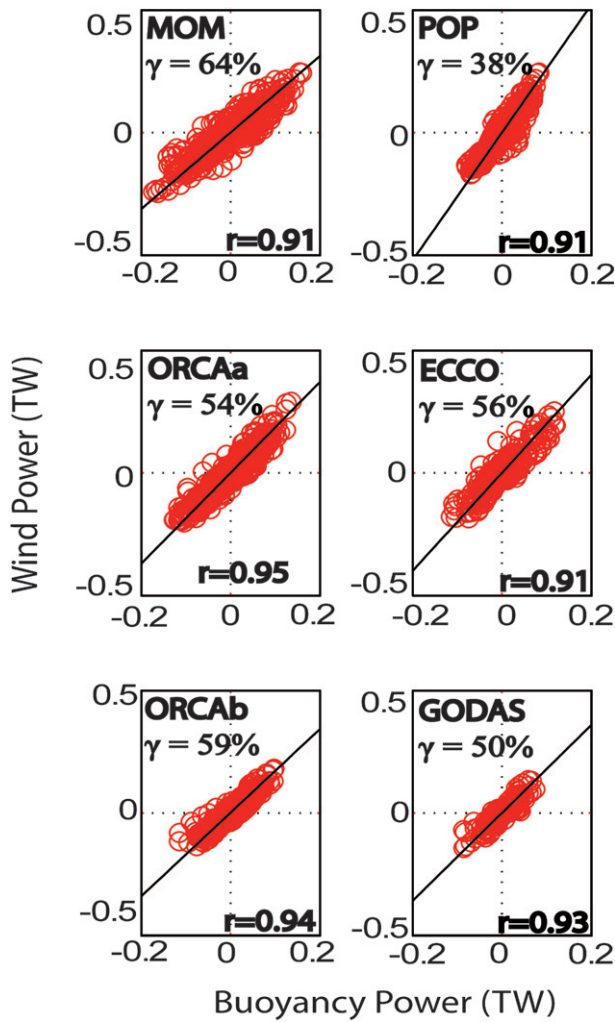


FIG. 6. Estimation of the efficiency γ of the wind power to buoyancy power conversion (both variables are measured in TW); γ^{-1} is calculated as the slope of the line given as the least squares fit between wind and buoyancy power anomalies. The correlation r between W and B is shown in the bottom right corner of each plot.

The damping coefficient α can be estimated via a least squares fit (Fig. 8) as

$$\alpha = \frac{\langle ED_2 \rangle}{\langle E^2 \rangle} \quad (9)$$

after a 5-point smoothing filter has been applied to the monthly data. The correlation coefficient between the energy loss D_2 and E ranges between 0.56 and 0.70 from one model to the next (Table 2), so it is indeed reasonable to assume, as the first-order approximation, that the diffusive dissipation is proportional to the available potential energy anomaly. Given such an approximation, the ORCAa model has an available potential energy damping rate of $\alpha = 0.36 \text{ s}^{-1}$ or, an e -folding damping time scale of $\alpha^{-1} = 0.9$ years.

TABLE 2. Summary of the energy-based metrics for the models and data assimilations. The Efficiency γ is defined as the fraction of wind power converted to the buoyancy power. The dissipation coefficient α gives the damping rate for available potential energy anomalies. The correlation coefficients between buoyancy power and wind power, and between diffusive energy loss and available potential energy are also shown.

Model	Efficiency γ	Correlation between B and W	Dissipation α^{-1} (yr)	Correlation between D_2 and E
ORCAa	54%	0.95	0.9	0.70
ORCAb	59%	0.94	1.0	0.59
MOM4	64%	0.91	1.0	0.68
POP	38%	0.91	1.2	0.59
GODAS	50%	0.93	—	—
ECCO	56%	0.91	1.2	0.56

Are the available potential energy damping rates consistent between models (Fig. 8)? It is interesting that despite some discrepancies in the efficiency between the ocean models, the available potential energy damping rates are robust and reasonably consistent values of α^{-1} range from 0.9 to 1.2 years.

The only exception is one of the data assimilation products, GODAS, with negative values of α . This seems unphysical and vastly different from the results of the other models and the ECCO data assimilation. These discrepancies occur most likely because ECCO and GODAS are very different types of data assimilations. ECCO is based on a freely running ocean model that conserves energy to the same extent as any ocean model (Wunsch and Heimbach 2007). In contrast, GODAS assimilates temperature and salinity, correcting the model data at each time step (Behringer 2007). Such a method can in effect introduce artificial sources and sinks of heat and freshwater and hence energy. By sacrificing energy conservation, GODAS can more easily align with observed currents. For this reason, it is not surprising that its available potential energy damping rates appear unphysical and so unlike our other results.

Using the shallow water equations to approximate the energy analysis above, the damping rate α can be related to the damping rate for thermocline anomalies (see appendix B and Fedorov 2007). The thermocline anomaly damping rate can be estimated as $(\alpha/2)^{-1}$, and the models studied here give its range between 1.8 and 2.4 years. This finding is generally consistent with the results of Fedorov (2007), who estimated this time scale at 2.3 ± 0.4 years using just one ocean model (MOM3). Fedorov (2007) assumed that the efficiency of wind power conversion was 100%, but this assumption did not affect the results, which were based on evaluating the phase shift between E and W .

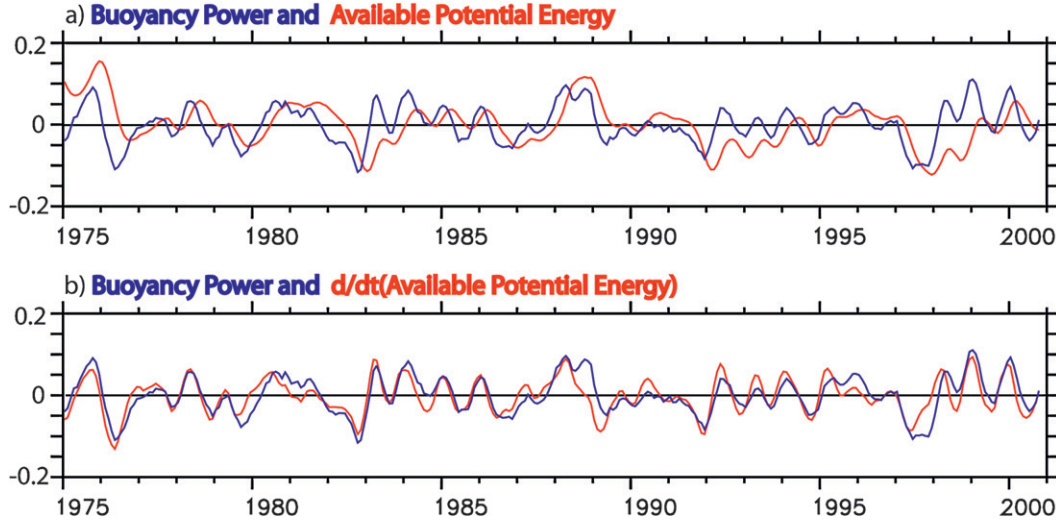


FIG. 7. The main components of the energy balance in Eq. (2) for the ORCAa model. (a) Monthly anomalies of buoyancy power (blue line; TW) and the available potential energy (red line; 10^{19} J). The buoyancy power leads the available potential energy by roughly 6 months. (b) The buoyancy power (blue line, TW) and rate of change of the available potential energy (red line, TW). Note the difference between the two, which indicates energy loss. Data have been smoothed with a 5-month running mean.

Combining the results on the efficiency and available potential energy damping, we can rewrite Eq. (3) with a good accuracy as

$$\frac{\partial E}{\partial t} = \gamma W - \alpha E, \quad (10)$$

where α is the damping coefficient¹ and γ is the efficiency constant (assuming that $B = \gamma W$). Now we can illustrate the role of the damping time scale α^{-1} . Following Fedorov (2007), let us assume that E and W can be described by two monochromatic functions:

$$W = W_o e^{i\omega t}; \quad E = E_o e^{i\omega(t-\Delta)}, \quad (11)$$

where Δ is the lag between E and W (positive when W leads E), $\omega = 2\pi/T$ is the oscillation frequency, and T is the oscillation period; W_o and E_o are both real numbers. If the damping coefficient α were zero ($\alpha^{-1} = \infty$), then W would lead E by a quarter period, and the value of the lag would be exactly $\Delta = T/4$.

Substituting expressions (11) into Eq. (10) yields a compatibility condition connecting Δ , ω , and α as

$$\text{Im}[(i\omega + 2\alpha)e^{-i\omega\Delta}] = 0. \quad (12)$$

After a little algebra, one can solve Eq. (12) for Δ :

$$\Delta = \left(\frac{T}{2\pi}\right) \arctan\left(\frac{2\pi}{\alpha T}\right). \quad (13)$$

¹ Note that Fedorov (2007) used a different notation with 2α as the coefficient in front of E in Eq. (10).

At low frequencies, for $T \gg 2\pi/\alpha$, we obtain $\Delta = \alpha^{-1}$. Thus, for low-frequency oscillations the damping time scale α^{-1} gives the lag between W and E . For high frequencies, when $T \ll 2\pi/\alpha$, we obtain for the lag $\Delta = T/4$.

5. Using energy metrics to understand model differences

Each of the models studied has a similar Niño-3.4 index (Fig. 9e), yet we have shown that their energy balances are different. To some extent, this can be explained by the implicit relaxation of surface temperatures to the observed SST, which occurs when surface heat fluxes are evaluated for forcing the models. However, by studying subsurface dynamics we can show how models can behave differently to get the same result. Let us consider three different cases to investigate how the models operate. ORCAa and ORCAb represent the same model, but forced with different wind stresses, with ORCAa having much stronger wind power variability than ORCAb (Fig. 9a). The POP model has a different, but similar magnitude, wind stress forcing as ORCAb (Maltrud and McClean 2005).

Both ORCA models convert a similar percentage of wind power (54%–59%) to buoyancy power (Table 2). This means that the variance of buoyancy power in ORCAb is weaker than in ORCAa. In the POP model, a much lower fraction of wind power (38%) is converted to buoyancy power, meaning that the variance of buoyancy power in POP is even weaker than that for the ORCAb run.

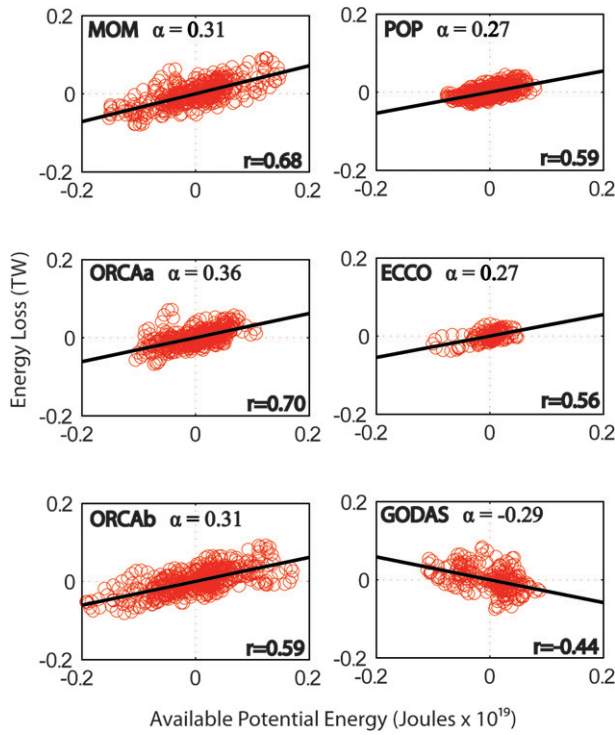


FIG. 8. Estimation of the damping rate α for the available potential energy. The damping rate α (10^{-7} s^{-1}) is calculated as the slope of the line given by the least squares fit between the energy loss D_2 (TW) and the available potential energy E (10^{19} J), see Eq. (2). The energy loss is estimated as the difference between the rate of change of available potential energy and buoyancy power and is described by D_2 in Eq. (2). The correlation coefficient r between the energy loss and the available potential energy is shown in the bottom right corner of each plot.

The buoyancy power then acts to alter the rate of change of available potential energy. The energy loss between the buoyancy power and the rate of change of available potential energy (Fig. 9c) is relatively small and its net result is to smooth the time series of B . The available potential energy (Fig. 9d) is a time integral of the previous two plots. Consequently, the available potential energy variability is larger for the ORCAa model than the ORCAb model. The POP model has even less variability.

The variance of the available potential energy is largely a measure of the thermocline slope anomalies at the equator and hence correlates highly with the Niño-3.4 temperature anomaly (Fig. 3b). Yet these models show that regardless of the magnitude of the available potential energy variations they generate, the Niño-3.4 index remains very similar (Fig. 9e). The question then arises: How can the Niño-3.4 indices be so similar if the magnitude of the available potential energy variance is so different? One of the reasons, we believe, lies in the mean depth of the equatorial thermocline produced by the models (Fig. 10).

The POP model, with weak available potential energy variability, has a very shallow equatorial thermocline, with tight density gradient. Only a small amount of energy is required to lift the thermocline sufficiently and induce a La Niña. Similarly, an El Niño requires a small decrease in the wind power and a small reduction in the available potential energy. At the other end of the scale, the ORCAa model (as well as MOM) has a deep thermocline. It takes far more buoyancy power in this case (and larger changes to available potential energy) to lift the thermocline during a La Niña event.

Thus, the models that have a deeper equatorial thermocline tend to have large available potential energy variations associated with steepening or leveling of the thermocline necessary to generate the required SST anomalies in the eastern equatorial Pacific. On the other hand, models with a shallower thermocline do not show large available potential energy variations. While the six models are not sufficient to calculate good statistics, it appears that they all fall on one line (Fig. 10).

6. Discussion and conclusions

We have explored the energy balance of the tropical Pacific Ocean on interannual time scales and developed two metrics for measuring energy dissipation in the tropical ocean that can be easily applied to any ocean-only or coupled model. These energy metrics incorporate subsurface ocean dynamics and give basinwide physical, integrated measures of the dissipation. This analysis will form the basis for the consideration of leading IPCC AR4 coupled model runs for the twentieth century in a companion paper (BRO). An assessment of the energetics of the mean state of the tropical ocean has been conducted in Brown and Fedorov (2008).

The ENSO cycle can be viewed as a cycle of gradual energy transformation (which suggests some similarities to the recharge–discharge oscillator theory; see Fig. 11). Wind power is generated at the surface of the ocean because of the wind stress acting on the surface currents. A fraction of this wind power (with the efficiency γ) is converted to buoyancy power. The buoyancy power determines the rate of change of the available potential energy, while the available potential energy reflects the displacement of the isopycnals. In the tropical Pacific the available potential energy is primarily associated with anomalies in the thermocline slope along the equator and hence acts as a proxy for the Niño-3.4 temperature anomaly. The final part of this energy loop (Fig. 11) comes from the wind stress response to the sea surface temperature anomaly.

We find that ocean models and data assimilations are approximately 50%–60% efficient in converting wind to

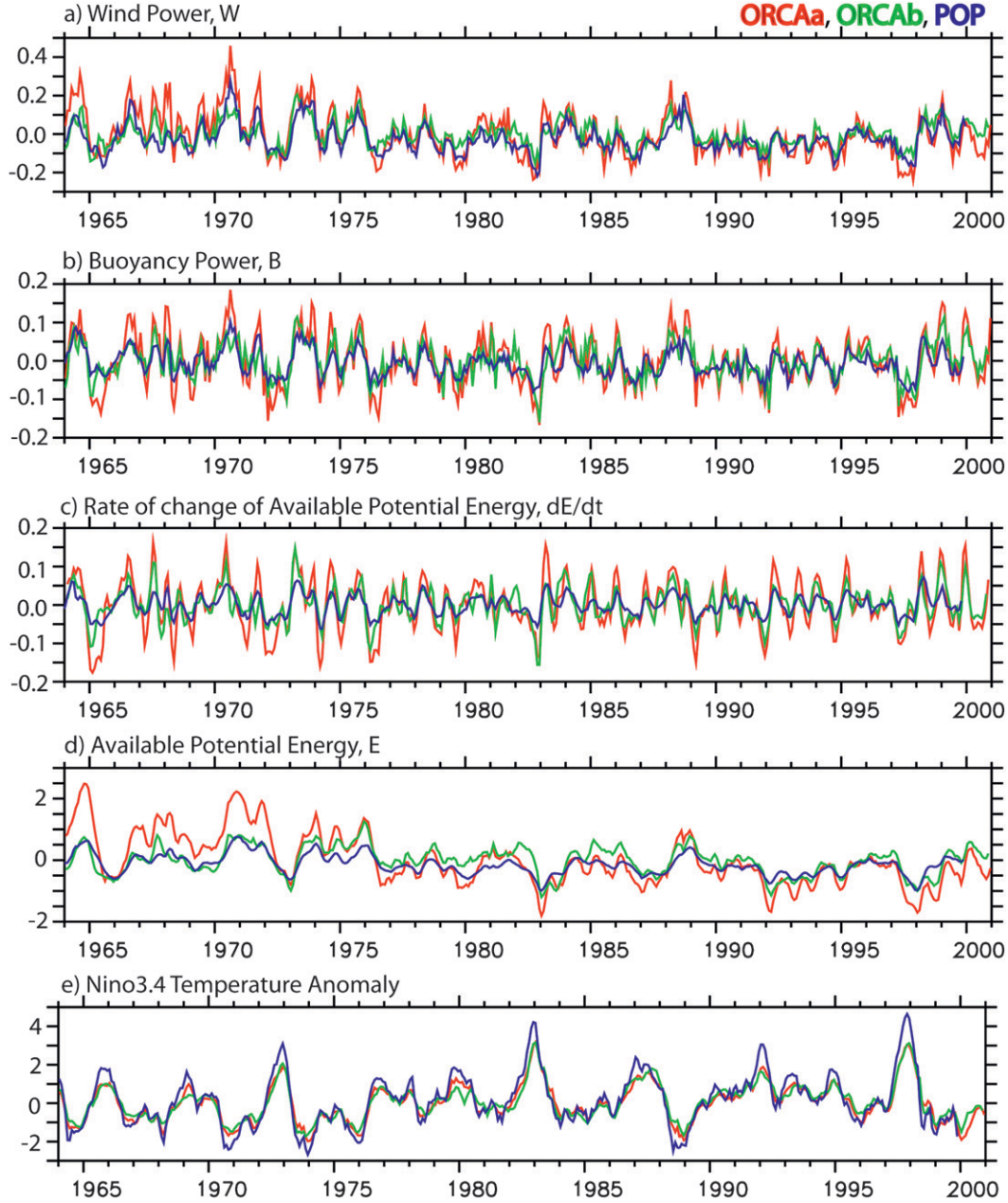


FIG. 9. Interannual variations in different components of the energy balance for three models, ORCAa (red), ORCAb (green), and POP (blue). (a) Wind power (TW), (b) buoyancy power (TW), (c) the rate of change of available potential energy (TW), (d) available potential energy (10^{19} J), and (e) Niño-3.4 temperature anomaly ($^{\circ}\text{C}$).

buoyancy power (i.e., $\gamma = 50\%–60\%$). Some models (such as POP) are less efficient in contrast to others (such as MOM). These discrepancies result from differences in friction schemes and, in part, different wind stress used to force the models (because vertical and horizontal shear in the ocean, and hence friction, depend on the details of the wind stress). A detailed consideration of these issues goes beyond the scope of this study and will be reported elsewhere.

We show that the available potential energy *e*-folding damping rate is estimated at approximately 1 year ($\alpha^{-1} = 1$ year). This is a robust result between the models and data assimilations generally consistent with the study of Fedorov (2007), who used the phase lag between E and W (generated by MOM3) to estimate this damping rate.

Based on an analogy with shallow-water equations, the damping rates for thermocline anomalies can be estimated at 2 years ($2\alpha^{-1} = 2$ years). This value gives

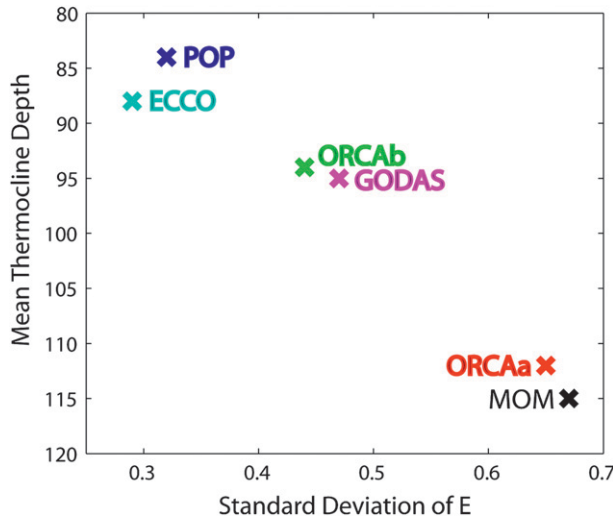


FIG. 10. Comparison of the mean thermocline depth (m) in the tropical basin and the standard deviation of available potential energy ($J \times 10^{19}$) for each model and data assimilation product. The mean thermocline depth is defined as the depth where $d\rho^*/dz$ is maximum. In POP this was not clearly defined and so the depth of an approximate isopycnal was used.

the lower bound on the decay time scale of the coupled ocean–atmosphere mode associated with ENSO. That is, the decay time scale of the coupled mode will be necessarily longer (or perhaps negative for an unstable mode) if positive feedbacks of ocean–atmosphere interactions are taken into account.

One of the processes contributing to energy dissipation in the tropical Pacific is related to tropical instability waves (Luther and Johnson 1990; Masina et al. 1999). Although this process is not explicitly explored within our energy analysis; the effect of tropical instability waves is fully included in the available potential energy equation [Eq. (19)], via explicitly resolved eddy diffusion, shear, and even thermal effects. The strength of our method is that it incorporates these processes (e.g., as part of model intercomparison), without the need to calculate them explicitly. We expect that the ability of each model to correctly represent these waves would feed back onto the energy budget and hence the ENSO representation; however, such analysis, while important, is beyond the scope of this study.

It is noteworthy that at this time available ocean observations are insufficient to conduct energy analysis similar to the one presented in this study and based on ocean models and data assimilations. To calculate available potential energy, it is necessary to have subsurface density data over the whole tropical band from 15°S to 15°N. At present the Tropical Atmosphere Ocean (TAO) array provide sufficient resolution only within 5° of the equator. Also, there are numerous spatial and temporal gaps in the TAO array

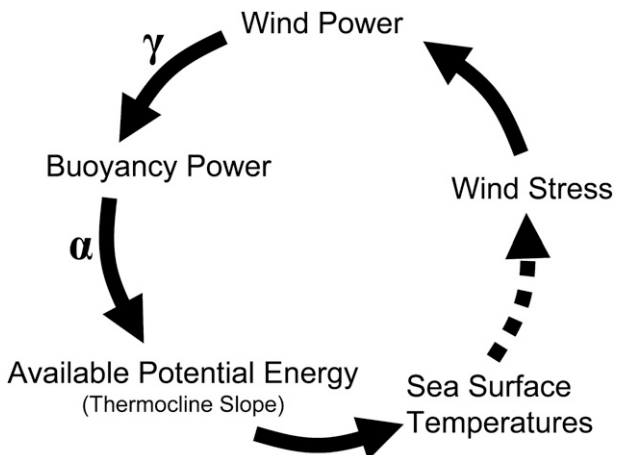


FIG. 11. A schematic of energy transfer and dissipation in the tropical ocean relevant for ENSO dynamics: Wind stress induces ocean currents, thus generating wind power anomalies. The wind power anomalies are converted to buoyancy power anomalies with the efficiency γ . Variations in buoyancy power modify the available potential energy (subject to the damping rate α). On ENSO time scales, available potential energy anomalies are related to changes in the thermocline slope along the equator and are proportional to SST anomalies in the eastern equatorial Pacific (a common index of ENSO). These SST anomalies then drive the wind stress changes as indicated by the dashed line (this part of the cycle is described by atmospheric processes and as such is not considered here).

data that make calculations of the available potential energy and even the thermocline depth inaccurate.

Similarly, there are large uncertainties in the wind power (when estimated from the observations). For example, Brown and Fedorov (2008) demonstrated that there is a large uncertainty in the mean wind power because of differences in the wind products. One possibility is to use satellite-derived Ocean Surface Current Analyses—Real Time (OSCAR) currents and wind stress (<http://www.oscar.noaa.gov/datadisplay/>); this is being explored at present, although their dataset is rather short. Huang et al. (2006) and Wunsch (1998) attempted to calculate wind power for the global ocean using different wind products and geostrophic currents calculated from altimeter data. Clearly, the geostrophic balance does not hold within a few degrees of equator, which does not allow us to use their approach for our analysis.

Overall, to conduct the analysis of energy dissipation, it is critical that wind stress and ocean density variations be consistent. Any mismatch between the two (because of inaccuracy of the observational data) will lead to artificial sinks or sources of energy. Although data assimilations provide the closest representation to observations, they too have many flaws. For example, as shown in this study, the GODAS dataset is not fully constrained by energy conservation. ECCO has been run for only a short period of time (15 years in our analysis).

In summary, we have developed a method to quantify oceanic energy dissipation as part of the overall energy balance in the tropical Pacific Ocean. This method provides easy-to-apply metrics for assessing gross energy dissipation relevant to ENSO. We have applied these metrics to a number of models and data assimilations to analyze the underlying physics of the subsurface ocean. Further, we argue that the energetics of the tropical ocean is a useful alternative to the common recharge oscillator approach to ENSO dynamics, since the energetics presents a basinwide integral approach that does not depend, for example, on choosing a particular isotherm to define the warm water volume of the ocean.

There are a number of other problems for which the energy analyses can become important. The impacts on ENSO of westerly wind bursts that frequently occur near the date line in the equatorial Pacific (e.g., Fedorov 2002; Fedorov et al. 2003) are one of the examples. By exploring the contribution of the bursts to wind power and the subsequent energy transfer to the thermocline, we can learn more about the development and predictability of ENSO events.

Acknowledgments. We thank Mat Maltrud for his tireless assistance setting up and running the POP model at Yale University. In addition, we thank Brian Dobbins for his help running and processing model data. We also thank Eric Guilyardi and Gurvan Madec for supply the ORCA data and advice, John Dunne for the MOM4 ocean model output, and Eric Guilyardi, Remi Tailleux, George Philander, and Lisa Goddard for discussions of this topic. ERA-40 data used in this study have been obtained from the ECMWF data server, <http://www.ecmwf.int/products/data/archive/descriptions/e4/>. The ECCO data assimilation was provided by the ECCO Consortium for Estimating the Circulation and Climate of the Ocean funded by the National Oceanographic Partnership Program (NOPP). We also thank NCAR for providing the NCEP Global Ocean Data Assimilation (GODAS) product.

This research is supported in part by grants to AVF from NSF (OCE-0550439), DOE Office of Science (DE-FG02-06ER64238, DE-FG02-08ER64590), the David and Lucile Packard Foundation, and CNRS (France).

APPENDIX A

The Kinetic Energy Equation and Available Potential Energy Equation

a. The kinetic energy equation

We begin with the horizontal momentum equations,

$$\begin{aligned} u_t + \mathbf{u} \cdot \nabla u - f v &= -\frac{p_x}{\rho} + (\mathbf{V}_{\text{MH}} u_x)_x + (\mathbf{V}_{\text{MH}} u_y)_y \\ &\quad + (\mathbf{V}_{\text{MV}} u_z)_z, \text{ and} \\ v_t + \mathbf{u} \cdot \nabla v + f u &= -\frac{p_y}{\rho} + (\mathbf{V}_{\text{MH}} v_x)_x + (\mathbf{V}_{\text{MH}} v_y)_y \\ &\quad + (\mathbf{V}_{\text{MV}} v_z)_z, \end{aligned} \quad (\text{A1})$$

where $\mathbf{u} = (u, v, w)$ is the 3D velocity field, p is pressure, ρ is density, $\boldsymbol{\tau} = (\tau^x, \tau^y)$ is wind stress and \mathbf{V}_{MV} and \mathbf{V}_{MH} are the vertical and horizontal eddy viscosities, respectively. The hydrostatic approximation is assumed. The boundary conditions are

$$\mathbf{V}_{\text{MV}} u_z \Big|_{z=0} = \frac{\tau^x}{\rho}, \quad \mathbf{V}_{\text{MV}} v_z \Big|_{z=0} = \frac{\tau^y}{\rho}, \quad u, v \rightarrow 0 \quad \text{as} \\ z \rightarrow -\infty. \quad (\text{A2})$$

By multiplying the zonal momentum equation by u , multiplying the meridional momentum equation by v , adding the two, and integrating over the volume of the tropical basin, one obtains

$$\frac{\partial K}{\partial t} = W - B - P - A_M - D_M, \quad (\text{A3})$$

where

$$\begin{aligned} K &= \iiint \hat{K} dV = \iiint \frac{\rho_0}{2} (u^2 + v^2) dV, \\ W &= \iint \mathbf{v} \cdot \boldsymbol{\tau} dA, \\ B &= \iiint \tilde{\rho} g w dV, \\ P &= \oint (p + p_s) \mathbf{u} \cdot \mathbf{n} d\sigma, \\ A_M &= \oint \hat{K} \mathbf{u} \cdot \mathbf{n} d\sigma, \quad \text{and} \\ D_M &= \iint \kappa_{\text{MV}} (\mathbf{v}_z \cdot \mathbf{v}_z) dV \\ &\quad + \iiint \kappa_{\text{MH}} [(\mathbf{v}_x \cdot \mathbf{v}_x) + (\mathbf{v}_y \cdot \mathbf{v}_y)] dV, \end{aligned} \quad (\text{A4})$$

with W being the wind power, B the buoyancy power, and $-P$ is the power generated by work done against pressure gradients by the ageostrophic flow. Also, A_M is the flux of kinetic energy through the walls of the tropical basin due to advection, and D_M is the energy dissipation due to friction induced by vertical and horizontal shear in the equatorial currents.

Note that here $\mathbf{v} = (u, v)$ are the horizontal components of current velocity. The wind power is integrated

over the surface of the tropical basin; other variables are integrated over the volume V or the walls of the basin boundary σ . Other terms are p_s the sea level pressure, and \mathbf{n} the unit vector out of the region. Potential density is given by $\tilde{\rho} = \rho - \rho^*$, with ρ^* being a horizontal average over the basin of interest (Fig. 1a) and ρ_o the mean background density.

In our study we group the last three terms of Eq. (A3), so that

$$D_1 = P + A_M + D_M, \quad (\text{A5})$$

which we refer to generally as dissipation.

b. The available potential energy equation

For this study we define the available potential energy as done in Margules (1905) and Lorenz (1955). In this definition the available potential energy is the difference between the total potential energy of a fluid and the potential energy of the same fluid mass in the same basin after an isentropic adjustment to a stable, exactly hydrostatic, reference state in which the isosteric and isobaric surfaces are level (Reid et al. 1981).

The available potential energy E (J), for brevity, is calculated in terms of density, according to Oort et al. (1989) as

$$E = \iiint \hat{E} dV = \iiint \frac{1}{2} \frac{\tilde{\rho}^2}{S^2} dV. \quad (\text{A6})$$

A stability factor S is introduced as $S^2 = |\rho_z^*/g|$, which differs from the buoyancy frequency by a factor of g^2/ρ^* , and $\tilde{\rho} = \rho - \rho^*$. A derivation of this expression for the available potential energy and its limitations can be found in Huang (1998, 2005).

The derivation of the available potential energy balance begins with the density equation, which is a consequence of the advection–diffusion equations for temperature and salt, with the same temperature and salt diffusivities, and a linear equation of state of seawater (Goddard and Philander 2000):

$$\tilde{\rho}_t + \mathbf{u} \nabla \tilde{\rho} + w \rho_z^* = \kappa_{\text{TH}} (\tilde{\rho}_{xx} + \tilde{\rho}_{yy}) + [\kappa_{\text{TV}} (\rho_z^* + \tilde{\rho}_z)]_z + Q_\rho, \quad (\text{A7})$$

where Q_ρ describes the effect of thermal and freshwater fluxes in the upper few layers of the model so that $Q_\rho = -\alpha_o Q_{\text{heat}} + \beta_o Q_{\text{salt}}$. The linear equation of state for seawater is written as $\rho = \rho_o - \alpha_o(T - T_o) + \beta_o(S - S_o)$, while κ_{TH} and κ_{TV} are the horizontal and vertical eddy diffusivities.

Potentially, one can use a nonlinear equation of state for seawater and different diffusivities for salt and tem-

perature (think double diffusion). In that case, the right-hand side of Eq. (A2) will acquire several additional terms that will eventually give rise to additional sources and sinks of energy in the available potential energy equation. However, for the very narrow range of temperature and salinity changes in the tropical ocean above 400 m, the errors of the linearized equation of state do not exceed more than a few percent (Goddard 1995). Nor would one expect big differences, if any, between eddy salt and temperature diffusivities for the large-scale motion in the tropical ocean.

Using Eq. (A2), Goddard and Philander (2000) then derive the rate of change of the available potential energy to be

$$\frac{\partial E}{\partial t} = B - Q - A_E - D_E, \quad \text{where} \quad (\text{A8})$$

$$\begin{aligned} Q &= - \iiint \left(\frac{\tilde{\rho}}{S^2} Q_\rho \right) dV, \\ A_E &= \oint (\mathbf{u} \hat{E}) \cdot \mathbf{n} d\sigma, \quad \text{and} \\ D_E &= - \iiint \left[\hat{E} w \left[\frac{\rho_{zz}^*}{(\rho_z^*)^2} \right] dV - \int \kappa_{\text{TH}} \nabla \hat{E} \cdot (\mathbf{i}, \mathbf{j}) d\sigma \right. \\ &\quad \left. + \iiint \frac{\kappa_{\text{TH}}}{S^2} [(\tilde{\rho}_x)^2 + (\tilde{\rho}_y)^2] dV \right. \\ &\quad \left. - \iiint \left\{ \frac{\tilde{\rho}}{S^2} [\kappa_{\text{TV}} (\tilde{\rho} + \rho^*)]_z \right\} dV \right], \end{aligned} \quad (\text{A9})$$

where B is the buoyancy power, A_E is the energy advection through the region boundary, and D_E is the total energy dissipation due to processes associated with vertical and horizontal diffusion (i.e., diffusive dissipation) or related to shear in the stability profile. Tropical instability waves (TIW), for example, contribute to this term. Here Q describes the effect of thermal and freshwater fluxes at the surface on the density field. The vertical integration for Q_ρ should be conducted over the few upper layers of the model. Surface heat fluxes dominate Q . On ENSO time scales they provide a negative feedback, warming the cold tongue during La Niña events and cooling during El Niño. Thus, this term contributes to damping of thermocline anomalies.

In a similar manner to the kinetic energy equation, for simplicity, we group the last three terms:

$$D_2 = Q + A_E + D_E. \quad (\text{A10})$$

Further details of the energy balance in the tropical Pacific can be found in Goddard and Philander (2000) and are discussed in Griffies (2004, chapter 5).

APPENDIX B

Energy Balance in the Shallow-Water Equations

A broad class of models used for studies and prediction of El Niño employ the reduced-gravity shallow-water equations for the ocean dynamics. These equations include viscous dissipation in the form of Rayleigh friction in the momentum equations and a similar damping term in the mass conservation equation that parameterizes entrainment of water across the thermocline caused by turbulent mixing. Frequently, the shallow-water equations are linearized and written in the long-wave approximation (e.g., Zebiak and Cane 1987):

$$u_t + g^*h_x - \beta yv = \frac{\tau}{\rho H} - \frac{\alpha_s}{2}u, \quad (\text{B1})$$

$$g^*h_y + \beta yu = 0, \quad (\text{B2})$$

$$h_t + H(u_x + v_y) = -\frac{\alpha_s}{2}h. \quad (\text{B3})$$

The notations are conventional, with u, v denoting the ocean currents, h and H denoting the local and mean depth of the thermocline, τ denoting the zonal wind stress, g^* denoting the reduced gravity, etc. The subscripts t, x , and y indicate the respective derivatives. The meridional wind stress can be also added to the equations, but it plays only a minor role in the energy balance. The typical boundary conditions for this system are no flow ($u = 0$) at the eastern boundary and no net flow ($\int u dy = 0$) at the western boundary. (Note that the main conclusions of this paper are based on the full Navier–Stokes equations of motion rather than the shallow-water equations.)

Following Gill (1980) and Cane and Patton (1984), in many applications it is assumed that the damping coefficient $\alpha_s/2$ has the same values in both continuity and momentum equations (which facilitates analytical treatment of this system), even though a priori the two coefficients are not required to be equal. This approach (i.e., adopting the same values for the damping coefficients) works fairly well as long as the damping is weak and one needs to account for dissipation only in some average sense. A question arises: what would be appropriate values of $\alpha_s/2$ to account for the tropical dissipation in a realistic setting?

Integrating Eqs. (B1)–(B3) yields an equation similar to Eq. (2):

$$\frac{\partial E}{\partial t} = W - \alpha_s E + \text{energy loss at boundaries}, \quad (\text{B4})$$

where

$$E = \frac{1}{2} \int \int \rho(Hu^2 + g^*h^2) dx dy \quad (\text{B5})$$

and

$$W = \int \int u\tau dx dy. \quad (\text{B6})$$

The integration in (B5) and (B6) is conducted over the tropical basin within the limits defined in this paper. The term proportional to $\alpha_s E$ describes explicit energy dissipation within the basin, while the term “energy loss at boundaries” corresponds to the net loss of energy at the southern, northern, and western boundaries (it can be easily shown that the long-wave approximation and the requirement of no net flow at the western boundary imply energy leakage through that boundary). This additional term in (B5) describes an implicit energy loss in the system (in contrast to the explicit loss described by α_s). At sufficiently low frequencies, for example, we expect the energy loss at boundaries to be relatively small and $\alpha_s \approx \alpha$.

REFERENCES

- AchutaRao, K., and K. R. Sperber, 2006: ENSO simulation in coupled ocean–atmosphere models: Are the current models better? *Climate Dyn.*, **27**, 1–15.
- Barnier, B., and Coauthors, 2006: Impact of partial steps and momentum advection schemes in a global ocean circulation model at eddy-permitting resolution. *Ocean Dyn.*, **56**, 543–567.
- Behringer, D. W., 2007: The Global Ocean Data Assimilation System (GODAS) at NCEP. Preprints, *11th Symp. on Integrated Observing and Assimilation Systems for Atmosphere, Oceans, and Land Surface*, San Antonio, TX, Amer. Meteor. Soc., 3.3. [Available online at www.ams.confex.com/ams/pdfs/papers/119541.pdf.]
- Blanke, B., and P. Delecluse, 1993: Variability of the tropical Atlantic Ocean simulated by a general circulation model with two different mixed-layer physics. *J. Phys. Oceanogr.*, **23**, 1363–1388.
- Brown, J. N., and A. V. Fedorov, 2008: Mean energy balance in the tropical Pacific Ocean. *J. Mar. Res.*, **66**, 1–23.
- , J. S. Godfrey, and R. Fiedler, 2007: A zonal momentum balance on density layers for the central and eastern equatorial Pacific. *J. Phys. Oceanogr.*, **37**, 1939–1955.
- Bryan, K., and L. J. Lewis, 1979: A water mass model of the World Ocean. *J. Geophys. Res.*, **84**, 2503–2517.
- Cane, M. A., and R. J. Patton, 1984: A numerical model for low-frequency equatorial dynamics. *J. Phys. Oceanogr.*, **14**, 1853–1863.
- Collins, W. D., and Coauthors, 2006: The Community Climate System Model version 3 (CCSM3). *J. Climate*, **19**, 2122–2143.
- Dawie, J. T., and L. Thompson, 2006: Effect of ocean surface currents on wind stress, heat flux, and wind power input to the ocean. *Geophys. Res. Lett.*, **33**, L09604, doi:10.1029/2006GL025784.
- Fedorov, A. V., 2002: The response of the coupled tropical ocean atmosphere to westerly wind bursts. *Quart. J. Roy. Meteor. Soc.*, **128**, 1–23.

- , 2007: Net energy dissipation rates in the tropical ocean and ENSO dynamics. *J. Climate*, **20**, 1108–1117.
- , and S. G. H. Philander, 2001: A stability analysis of the tropical ocean–atmosphere interactions: Bridging measurements of, and theory for, El Niño. *J. Climate*, **14**, 3086–3101.
- , and J. Brown, 2009: Equatorial waves. *Encyclopedia of Ocean Sciences*, 2nd ed., J. Steele, Ed., Academic Press, 3679–3695.
- , S. L. Harper, S. G. Philander, B. Winter, and A. T. Wittenberg, 2003: How predictable is El Niño? *Bull. Amer. Meteor. Soc.*, **84**, 911–919.
- Gill, A. E., 1980: Some simple solutions for heat-induced tropical circulation. *Quart. J. Roy. Meteor. Soc.*, **106**, 447–462.
- Goddard, L., 1995: The energetics of interannual variability in the tropical Pacific Ocean. Ph.D. dissertation, Princeton University, 210 pp.
- , and S. G. Philander, 2000: The energetics of El Niño and La Niña. *J. Climate*, **13**, 1496–1516.
- Griffies, S. M., 2004: *Fundamentals of Ocean Climate Models*. Princeton University Press, 518 pp.
- , and Coauthors, 2005: Formulation of an ocean model for global climate simulations. *Ocean Sci.*, **1**, 45–79.
- Guilyardi, E., 2005: El Niño–mean state–seasonal cycle interactions in a multi-model ensemble. *Climate Dyn.*, **26**, 329–348.
- , A. Wittenberg, A. Fedorov, M. Collins, C. Wang, A. Capotondi, G. J. van Oldenborgh, and T. Stockdale, 2009: Understanding El Niño in ocean–atmosphere general circulation models: Progress and challenges. *Bull. Amer. Meteor. Soc.*, **90**, 325–340.
- Huang, R. S., 2004: Energy flows in the ocean. *Encyclopedia of Energy*, Elsevier, 497–509.
- Huang, R. X., 1998: Mixing and available potential energy in a Boussinesq ocean. *J. Phys. Oceanogr.*, **28**, 669–678.
- , 2005: Available potential energy in the world's oceans. *J. Mar. Res.*, **63**, 141–158.
- , W. Wang, and L. L. Liu, 2006: Decadal variability of wind-energy input to the world ocean. *Deep-Sea Res. II*, **53**, 31–41.
- Jin, F.-F., 1997: An equatorial ocean recharge paradigm for ENSO. Part I. Conceptual model. *J. Atmos. Sci.*, **54**, 811–829.
- Kao, H.-Y., and J.-Y. Yu, 2009: Contrasting eastern Pacific and central Pacific types of ENSO. *J. Climate*, **22**, 615–632.
- Large, W. G., J. C. McWilliams, and S. C. Doney, 1994: Oceanic vertical mixing – A review and model with a nonlocal boundary-layer parameterization. *Rev. Geophys.*, **32**, 363–403.
- Lorenz, E. N., 1955: Available potential energy and the maintenance of the general circulation. *Tellus*, **7**, 157–167.
- Luther, D. S., and E. S. Johnson, 1990: Eddy energetics in the upper equatorial Pacific during the Hawaii-to-Tahiti Shuttle Experiment. *J. Phys. Oceanogr.*, **20**, 913–944.
- Maltrud, M. E., and J. L. McClean, 2005: An eddy resolving global 1/10° ocean simulation. *Ocean Modell.*, **8**, 31–54.
- Margules, M., 1905: Über die energie der stürme. *Jahrbuch Zentralanstalt für Meteorologie und Geodynamik*, 1–26.
- Masina, S., S. G. H. Philander, and A. B. G. Bush, 1999: Analysis of tropical instability waves in a numerical model of the Pacific Ocean. Part II: Generation and energetics of the waves. *J. Geophys. Res.*, **104**, 29 637–29 661.
- McPhaden, M. J., S. E. Zebiak, and M. H. Glantz, 2006: ENSO as an integrating concept in Earth science. *Science*, **314**, 1740–1745.
- Meinen, C. S., and M. J. McPhaden, 2000: Observations of warm water volume changes in the equatorial Pacific and their relationship to El Niño and La Niña. *J. Climate*, **13**, 3551–3559.
- Oort, A. H., S. C. Ascher, S. Levitus, and J. H. Peixoto, 1989: New estimates of the available potential energy in the world ocean. *J. Geophys. Res.*, **94**, 3187–3200.
- Reid, R. O., B. A. Elliot, and D. B. Olson, 1981: Available potential energy: A clarification. *J. Phys. Oceanogr.*, **11**, 15–29.
- Wang, C., S. P. Xie, and J. A. Carton, 2004: *Earth's Climate: The Ocean–Atmosphere Interaction*. *Geophys. Monogr.*, Vol. 147, Amer. Geophys. Union, 405 pp.
- Wang, W., and R. X. Huang, 2004: Wind energy input to the Ekman layer. *J. Phys. Oceanogr.*, **34**, 1267–1275.
- Weijer, W., and S. T. Gille, 2005: Energetics of wind-driven barotropic variability in the Southern Ocean. *J. Mar. Res.*, **63**, 1101–1125.
- Wunsch, C., 1998: The work done by the wind on the oceanic general circulation. *J. Phys. Oceanogr.*, **28**, 2332–2340.
- , and P. Heimbach, 2007: Practical global oceanic state estimation. *Physica D*, **230**, 197–208.
- Zebiak, S. E., and M. A. Cane, 1987: A model El Niño–Southern Oscillation. *Mon. Wea. Rev.*, **115**, 2262–2278.
- Zhai, X. M., and R. J. Greatbatch, 2007: Wind work in a model of the northwest Atlantic Ocean. *Geophys. Res. Lett.*, **34**, L04606, doi:10.1029/2006GL028907.